Wiley
International Journal of Energy Research
Volume 2025, Article ID 2898099, 12 pages
https://doi.org/10.1155/er/2898099

WILEY

Research Article

Highly Sensitive, Thin, and Conformal MoS_2 Thermistors for In Situ Thermal Characterization of Lithium-Ion Batteries

Dianhong Huo and Jungwook Choi

School of Mechanical Engineering, Chung-Ang University, Seoul 06974, Republic of Korea

Correspondence should be addressed to Jungwook Choi; choij@cau.ac.kr

Received 12 February 2025; Revised 11 June 2025; Accepted 28 June 2025

Academic Editor: Puran Pandey

Lithium-ion batteries (LIBs) experience continuous temperature changes during operation and can overheat due to overcharging and short circuits, leading to severe safety hazards, such as thermal runaway. As temperature during the operation is a direct indicator of the safety status of LIBs, developing a high performance thermistor that is capable of sensitively monitoring the temperature changes of LIBs in real time is crucial. In this study, we developed, fabricated, and evaluated a highly sensitive, thin, and flexible temperature sensor composed of 2D MoS_2 as a thermosensitive material. The sensor can be conformally integrated onto the surface of LIBs without interfering with the assembly of other components. The MoS_2 thermistor exhibits a high temperature coefficient of resistance (TCR) of −1.94%/°C (corresponding thermal sensitivity is 200 mV/°C) with a high linearity (R^2 of 0.98) in the 20–60°C temperature range. This sensitivity is three to four orders of magnitude higher than that of thermocouples (usually tens of μV/°C) that are conventionally used for the temperature monitoring of LIBs. Moreover, the MoS_2 thermistor exhibits an insignificant response to bending, with resistance changes of less than 0.3% under a bending angle of 40°, which the sensor could experience owing to LIB swelling during operation. The spatial temperature changes of LIBs during their charge-discharge cycles can also be monitored accurately in real time by integrating multiple MoS_2 thermistors. Our thermistor provides sensitivity, stability, simplicity, and portability, which are critical for the continuous thermal characterization of LIBs and the reduction of the risk of thermal runaway.

1. Introduction

Lithium-ion batteries (LIBs) are reliable, long-lasting, and high-energy density storage systems that are widely used in diverse applications ranging from portable electronic devices to electric vehicles [1–3]. Consequently, as the demand for these devices increases, the energy and power densities of LIBs must also be improved continuously. However, as LIB energy performance increases, the safety risks also rise significantly [4, 5]. One of the most significant limitations of LIBs is that they must operate within a relatively narrow temperature range. LIBs release heat during charging and discharging, and the average working temperature for LIBs is usually between 20 and 60°C [6–8]. However, once the operating temperature increases beyond a specific critical level, the LIB may experience thermal runaway, eventually swelling and then exploding [9, 10]. Other potential causes of thermal runaway include overheating, overcharging, excessive charge and discharge rates, short circuits, and physical damage, such as punctures [11–13]. Thermal runaway can result in catastrophic outcomes including fire, explosion, and toxic gas release, posing significant risks to both users and surrounding infrastructure [14, 15]. A critical early indicator of thermal runaway is the rate of temperature change within the LIB [16, 17]. Therefore, a high performance sensor that can accurately monitor temperature changes in LIBs in real time must be developed.

Thermocouples are typically employed for measuring the temperature of LIBs. These devices are usually encased in epoxy resin and either attached to or inserted within the battery. However, the low sensitivity and nonlinear output of thermocouples limit their temperature-sensing performance [18, 19]. In addition, thermocouples require continuous calibration against hot and cold reference junctions and, when integrated

inside an LIB, are not stable under active electrochemical reactions and require tight packaging, which increases their cost [20–22]. To determine the spatial temperature distribution of LIBs, multiple thermocouples must be integrated, which is labor-intensive and produces that can yield unreliable measurements. On the other hand, infrared (IR) thermometers can provide noncontact temperature distribution measurements with a high sensitivity; however, IR cameras are bulky and expensive, making their integration into portable LIBs impractical [23–24]. Moreover, IR imaging requires careful calibration for long-term temperature tracking because the measurement accuracy can be affected by external interference, such as radiation from the atmosphere and neighboring objects during operation [24, 26]. Otherwise, fiber Bragg grating sensors provide a linear temperature response when integrated into batteries but are susceptible to electric crosstalk [27–29]. In addition, such sensors need to be tethered to the current collector, and the fiber must penetrate the cathode and separator through the battery housing, thus compromising the integrity and performance of the battery [19, 21]. In terms of manufacturing, sensor installation complicates LIB assembly processes and may increase safety risks. Therefore, resistive temperature detectors, which are advantageous of simple measurement scheme, with a high sensitivity, broad detection range, fast response, cost-effectiveness, and stability that can be attached conformally to the surface of LIBs without constraints are required for LIB thermal characterization [30–34].

To achieve a high sensitivity and accurate temperature measurements, various nanomaterials have been employed as thermosensitive materials, including carbon nanomaterials [10, 35–37], metals and metal oxides, such as Ag and ZnO nanowires [38, 39]. These materials exhibit temperature sensitivity, quantified as the temperature coefficient of resistance (TCR), typically ranging from 0.4% to 0.6%/°C [38, 39]. To explore novel materials with enhanced sensitivity, composites comprised of carbon nanotubes (CNTs) and MXenes have been evaluated for temperature monitoring of batteries and the human body; however, their TCR only reached 0.5%/°C [40]. On the other hand, atomically thin semiconductors, such as MoS_2 have emerged as excellent thermosensitive materials for flexible sensors [41, 42]. Given its unique structural, mechanical, and electrical characteristics along with the availability of large-scale processing techniques [43], MoS_2 has been successfully integrated into various types of temperature sensors, such as fiber-optic sensors (0.1211 dB/°C) [44], multiwalled CNT–MoS_2 nanocomposite temperature sensors (−0.62%/°C) [45], graphene–MoS_2 thermoelectric devices (21 μV/°C) [46], and monolayer MoS_2-based flexible sensors (~1.5%/°C) [47]. These studies collectively demonstrate that MoS_2 exhibits a rapid thermal response and the high sensitivity necessary for temperature monitoring. Nevertheless, the application of MoS_2-based sensors for LIB temperature monitoring has not yet been explored, and the temperature sensitivity of MoS_2 can be further improved by modulating its morphology. Therefore, sensitive, thin, and flexible MoS_2 thermistor sensors must be designed and evaluated for accurate LIB temperature monitoring and early detection of thermal runaway.

In this paper, we present thin and flexible thermistors for LIBs based on 2D MoS_2 that can be conformally attached to a battery surface for the first time. The thermistor was fabricated by spray-coating a MoS_2 dispersion onto patterned electrodes on a flexible polyimide (PI) substrate. Simple, scalable, and reproducible processes were used to minimize the manufacturing costs and performance variations among the fabricated sensors (less than 0.04%). The sensor exhibits a high TCR (−1.94%/°C) (corresponding to a thermal sensitivity of 200 mV/°C) and cyclic sensing repeatability (deviation of less than 0.22%). By attaching the MoS_2 thermistor to the LIB surface, temperature changes during 0.5 C and 1 C-rate charge−discharge cycles could be accurately measured and recorded, while thermocouples and an IR camera provided reference data for comparison. Furthermore, the high sensitivity and adaptability of the MoS_2 thermistor enabled real time spatial temperature mapping of LIBs during charge−discharge cycles, demonstrating the feasibility of continuous thermal characterization.

2. Materials and Methods

2.1. Materials. Poly (pyromellitic dianhydride-co-4,4-oxydianiline) (Sigma-Aldrich), amic acid solution (P [PMDA-ODA]) (12.8 wt%, Sigma-Aldrich) were used for preparation of PI substrate. PMMA (Poly [methyl methacrylate]) powder (average MW ≈ 350000, Sigma-Aldrich), molybdenum (IV) sulfide powder (99% purity, 325 mesh, Alfa Aesar), negative photoresist (DNR-L300-40, 120CP, DongJin), Au pellet (99.99% purity, iTASCO), and Cr pellet (99.99% purity, iTASCO) were used for the fabrication of the MoS_2 thermistor. All chemicals and materials were used as received.

2.2. Fabrication of Substrate and Electrode. The PMMA solution was spin-coated onto a clean Si wafer at 1200 RPM for 30 s and subsequently heated to 120°C for 15 min to form a PMMA film. A P(PMDA-ODA) solution was then spin-coated onto the PMMA layer at 2000 RPM for 30 s, followed by soft baking in a vacuum oven at 80°C. This process was repeated to form multilayer imidized PI films. The PI layer was then cured at 140°C for 4 h. Photolithography was used to define the electrode patterns on the PI surface, and electron beam evaporation was used to deposit 100-nm-thick Au with a 20-nm-thick Cr adhesion layer. Finally, the interdigitated (IDT) electrodes were defined by liftoff in acetone.

2.3. MoS_2 Preparation and Coating. The MoS_2 powder was ground in a mortar for 30 min and dispersed in acetone using a tip sonicator (SONOPULS, BANDELIN) for 5 h at an amplitude of 16.4 μm. The MoS_2 dispersion was then centrifuged at 1000 RPM for 20 min (Rotina 380, Hettich), and the supernatant was used to ensure uniformity and long-term stability. The MoS_2 dispersion was then coated evenly onto the PI substrate with patterned IDT electrodes using a spray gun through a shadow mask. Finally, the MoS_2-coated substrate was annealed at 180°C under an inert atmosphere for 2 h to remove the solvent completely.

2.4. Device Characterization. The MoS_2 thermistor characteristics were measured using the following systems and

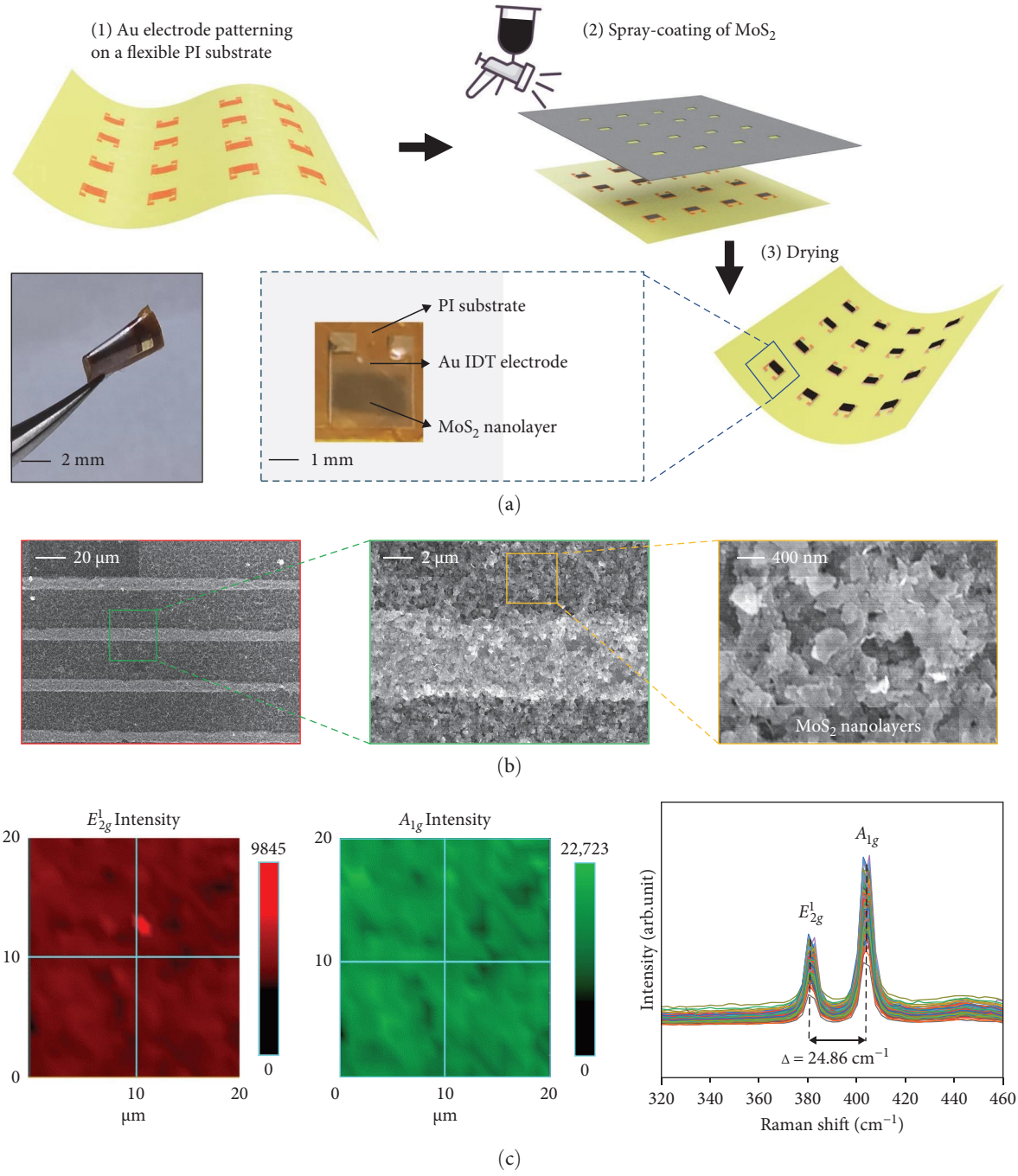

FIGURE 1: (a) Schematic of the manufacturing process and photographs of the fabricated MoS_2 thermistor. (b) SEM images of uniformly coated MoS_2 nanolayers on both IDT electrodes (brighter regions) and the PI substrate (darker regions). (c) Raman intensity maps for the E^1_{2g} and A_{1g} peaks of MoS_2 deposited onto the PI substrate, along with the corresponding Raman spectra.

techniques: The current–voltage (I–V) curves and the relative resistances of the MoS_2 thermistors were recorded utilizing a source meter (2450, Keithley). The surface morphology of MoS_2 nanomaterials was observed using scanning electron microscopy (SEM; SIGMA 300 Carl Zeiss), and Raman spectra were acquired utilizing a Raman spectrometer (XploRA Plus, Horiba) under a 100× focus lens and a 532-nm laser, featuring a spot diameter of 1 μm. Battery charging and discharging were performed using a battery test system (BaSytEC XCTS). The surface temperatures of the batteries were assessed utilizing thermocouples and IR cameras (FLIR CX200).

3. Results and Discussion

3.1. Fabrication and Characterization of MoS_2 Thermistor. Figure 1 shows the schematic and structural details of the flexible MoS_2 thermistor. The MoS_2 thermistor was fabricated by

standard micropatterning of electrodes onto a PI substrate, followed by spray-coating of the MoS_2 dispersion, as shown in Figure 1a. As detailed in Figure S1, the process begins by coating a Si wafer with PMMA and PI, where PMMA serves as a sacrificial layer for releasing the PI substrate from the wafer. The thickness of the PI substrate was less than 100 μm to ensure conformal contact with the LIB surface. Photolithography, electron beam evaporation of Au, and liftoff process were used to define an IDT electrode array on the PI surface. Simultaneously, the MoS_2 nanolayers were exfoliated and stably dispersed in acetone (0.6 mg/mL) through tip sonication and followed by centrifugation. The MoS_2 dispersion was uniformly spray-coated onto the IDT electrodes using a shadow mask, subsequently dried. The inset photograph in Figure 1a (outlined by dashed lines) shows the fabricated MoS_2 thermistor. The fabrication processes of flexible MoS_2 thermistors are simple, reliable, and reproducible, thereby ensuring minimal performance variations between the manufactured sensors. In addition, the high flexibility of the sensor enables it to bend and fold easily without damage (inset in Figure 1a), making the sensor suitable for LIB surface contact measurements. The SEM images show the morphology of the MoS_2 sensing layer coated on the IDT electrodes and the PI substrate after thermal treatment under an inert atmosphere (Figure 1b). The MoS_2 nanolayers are tightly packed and overlapped with each other, forming an electrical pathway with numerous interflake contacts between the electrodes with an average lateral MoS_2 flake size of ~ 466 ± 22 nm (Figure S2). The thickness of coated MoS_2 layer was ~ 100 nm (Figure S3). In our MoS_2 sensing layer, the electron transport is controlled by hopping between the MoS_2 flakes, indicating that the hopping transport in the MoS_2 layer is likely to lead to a large TCR [42]. Raman spectroscopy was used to further analyze the MoS_2 sensing layer. MoS_2 has two characteristic phonon modes: E^1_{2g}, corresponding to in-plane vibrations of the sulfur and molybdenum atoms perpendicular to each other in the plane, and A_{1g}, associated with out-of-plane vibrations of sulfur atoms [48, 49]. Multilayer MoS_2 exhibits both interlayer and interlayer vibrations, which are caused by the restoring forces generated by van der Waals interactions [50, 51]. The corresponding interlayer modes in multilayer MoS_2 strongly depend on its thickness, and the peak positions of the E^1_{2g} and A_{1g} modes can be used to identify the number of layers of MoS_2 flakes [52]. As shown in the Raman spectra in Figure 1c, the peak position difference between E^1_{2g} (383.6/cm) and A_{1g} (408.5/cm) was 24.86/cm, indicating that the bulk MoS_2 was successfully exfoliated and multilayer MoS_2 was coated onto the substrate [48, 50, 53]. Importantly, as shown in the Raman intensity map over an area of 400 μm^2 in Figure 1c, the positions and intensities of the two characteristic peaks (E^1_{2g} and A_{1g}) of the multilayer MoS_2 are uniform across the area. This proves the uniformity of the MoS_2 dispersion and spray-coating process.

3.2. Sensing Performance of MoS_2 Thermistor. Figure 2a shows the temperature-dependent *I–V* characteristics of the MoS_2 thermistor, which exhibit linear behaviors over a broad temperature range of 20–160°C. As the temperature increased, the resistance of MoS_2 decreased significantly from 0.68 MΩ at 20°C to 0.01 MΩ at 160°C owing to the semiconducting properties of MoS_2. The temperature-sensitive conduction mechanism of MoS_2 can be attributed to the thermal excitation of electrons near the Fermi level resulting from the temperature increase. This excites valence electrons to the conduction band, enhancing electrical conduction and resulting in temperature-dependent resistance changes [54–56]. The relative resistance change ($\Delta R/R_0$) of MoS_2 with respect to the temperature is shown in Figure 2b, where ΔR is the change in resistance at a given temperature and R_0 is the initial resistance at the baseline temperature. The temperature sensitivity of the MoS_2 thermistor can be divided into three linear regions, whereby the slope indicates the TCR. The peak TCR observed between 20 and 60°C was −1.94%/°C with high linearity ($R^2 = 0.98$). This temperature range covers the typical operating temperature range of commercial LIBs. In addition, the thermal sensitivity was calculated to be 200 mV/°C based on the TCR and input current, which is a few orders of magnitude higher than that of a typical commercial thermocouple (usually tens of μV/°C). The high thermal sensitivity can be attributed to the morphology of the MoS_2 layer, where stacked structures facilitate contact-dominated hopping transport [57–60]. Notably, MoS_2 exhibited the highest TCR among various temperature-sensitive materials under identical sensor preparation and measurement conditions in the 20–60°C temperature range (Figure S4a). It is also noted that our MoS_2-based thermistor exhibits a higher sensitivity, and a wider sensing range compared to previously reported sensors for the thermal characterization of LIBs (Table S1). To the best of our knowledge, this is the first demonstration of an MoS_2-based flexible thermistor applied to LIB thermal monitoring. Moreover, TCR was dependent on the amount of MoS_2 coated onto the IDT electrodes (Figure S4b). Although a small amount of MoS_2 (e.g., 2 mg) also exhibits a high TCR (−1.85%/°C), the mass of the MoS_2 coating was set to 12 mg in this study to maximize the temperature sensitivity. While the TCR was not directly evaluated as a function of layer thickness or electrode gap distance, the observed dependance on MoS_2 coating mass (Figure S4b) suggests that increasing the layer thickness or electrode gap—which would both require more MoS_2—could further enhance the TCR. This effect likely arises from increased interfacial resistance paths between stacked flakes, which dominate charge transport in our multilayer configuration.

The MoS_2 thermistor exhibited stability with a low signal noise, enabling the detection of subtle temperature variations as low as 0.4°C, as shown in Figure 2c. The ability of the sensor for continuous and stable temperature monitoring over prolonged periods was also evaluated by increasing the temperature in 1°C increments. Given the negative TCR and linearity, the resistance of the sensor decreased monotonically as the temperature increased stepwise (Figure S5a). Furthermore, the sensor exhibited small resistance changes of less than 0.3% under bending angles of up to 40°, both at 25 and 45°C (Figure 2d). The high flexibility and minimal bending response of the MoS_2 thermistor suggests its potential applicability to various LIB types including cylindrical cells. Considering the high TCR, the change in resistance upon bending is negligible, enabling the sensor to remain conformally attached to the battery, even

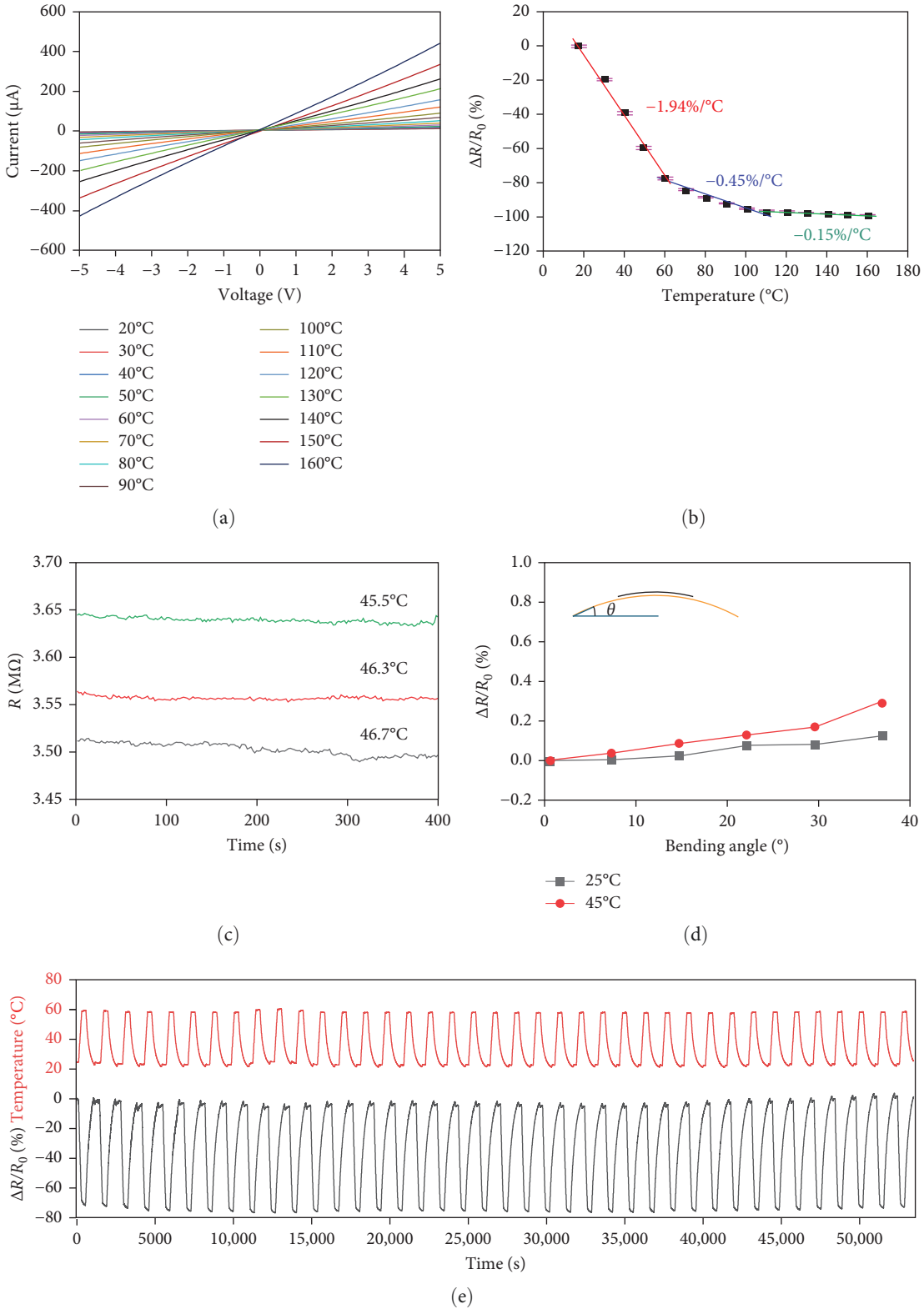

FIGURE 2: (a) Linear I–V curves of the MoS_2 thermistor at different temperatures ranging from 20 to 160°C. (b) Measured TCR of the MoS_2 thermistor, exhibiting a high TCR of −1.94%/°C in the 20–60°C temperature range. The error bars represent the standard deviation obtained from three different samples. (c) Signal stability of the MoS_2 thermistor with subtle differences in temperature. (d) Minimal response of the MoS_2 thermistor at less than 0.3% upon bending at different temperatures. (e) Resistance changes of the MoS_2 thermistor under repeated heating and cooling cycles for over 15 h.

when the LIB swells during charging and discharging. Typical thickness expansion of LIBs during standard cycling is in the range of 0.2% to 3.5%, while severe swelling under abusive conditions may reach several millimeters [10, 61, 62]. As the 40° bending angle applied in our experiment corresponds to vertical displacement of ~ 2.1 mm, the sensor would show negligible resistance change under a deformation comparable to abnormal swelling expected in practical prismatic LIBs. To verify the measurement repeatability of the MoS_2 thermistor, the resistance change was recorded as the temperature was increased from 20 to 160°C, demonstrating consistent responses over multiple cycles of temperature changes (Figure S5b). The high repeatability of resistance change under thermal cycling validates the accuracy and stability of the MoS_2 thermistor for reliable temperature sensing. Moreover, as shown in Figure 2e, thermal cycling for more than 15 h demonstrated the excellent stability of the MoS_2 thermistor, and its resistance varied correspondingly to temperature changes between 20 and 60°C. The reproducibility of the fabrication process for the MoS_2 thermistor was also validated by measuring the TCR across three different sensors. The TCR values are $-1.94 \pm 0.005\%/°C$, $-0.45 \pm 0.004\%/°C$, and $-0.15 \pm 0.002\%/°C$ in the 20–60°C, 60–110°C, and 110–160°C temperature ranges, respectively, verifying the possibility of a large-area sensor array composed of multiple MoS_2 thermistors that can measure the spatial temperature distribution of LIBs sensitively in a repeatable manner (Figure S5c). Notably, this sensing range (20–160°C) encompasses all key thermal transition stages associated with thermal runaway, suggesting that the MoS_2 thermistor may serve as an effective tool for early stage warning of LIB failure.

3.3. Application for LIB Thermal Monitoring. Real time temperature monitoring of an LIB during charge and discharge cycles of 0.5 and 1 C by the MoS_2 thermistor was verified (Figure 3). The experimental setup consisted of a thermostatic chamber, in which the LIB was connected to battery charge-discharge equipment. The specific parameters of the LIB used in this study are summarized in Table S2. The MoS_2 thermistor was conformally attached to the LIB surface and shielded with a PI film to minimize interference. In this configuration, the MoS_2 layer faces the battery surface for direct thermal contact, while the PI substrate functions as an encapsulation layer to block environmental interferences, such as humidity and oxygen. In addition, intrinsic oxidation resistance of MoS_2 would ensure stability during operation [63, 64]. A source meter continuously recorded the resistance change of the MoS_2 thermistor throughout LIB charge-discharge cycles, while a thermocouple was attached to the MoS_2 thermistor as a reference. To ensure measurement accuracy, the thermostatic chamber stabilized the environmental temperature. The LIB voltage changes during the charge and discharge cycles are shown in Figure 3a,b. Upon reaching full charge, the LIB was discharged at a constant current (e.g., 4 A for 1 C-rate) until it reached a terminal voltage of 2.5 V. A subsequent pause permitted the LIB temperature to stabilize under ambient conditions, clearly distinguishing temperature variations from discharging and charging processes. When the surface temperature had returned to its initial state, the LIB was charged again at a constant current of 4 A (at 1 C-rate) until the terminal voltage reached 4.2 V. Charging was then switched to a constant voltage until the current fell below the critical current (0.02 A), indicating a full charge.

Heat is generated during the LIB charge and discharge cycles as a result of both Joule heating caused by internal resistance and entropy changes during redox reactions [65, 66]. The heat generated inside an LIB is transferred to the surface, and the surface temperature indicates the state of internal heat transfer and external cooling [67, 68]. The MoS_2 thermistor responded sensitively to changes in the temperature on the LIB surface. During constant-current charging and discharging, high currents lead to significant increases in the temperature [67, 69]. Given the negative TCR of MoS_2, its resistance decreases as the surface temperature increases. Conversely, during constant voltage charging, the lower current results in the cooling rate exceeding the heating rate [70, 71], causing the surface temperature to gradually decrease and the resistance of the sensor to increase, as shown in Figure 3c,d. The resistance change of the MoS_2 thermistor is converted to the temperature based on the measured TCR. At a low discharge rate (0.25 C), insufficient entropic heat was generated and a significant temperature change on the LIB surface was not caused [65, 71]. As such, the LIB temperature fluctuated as the thermostatic chamber continuously balanced the temperature, and this temperature fluctuation was also sensitively monitored using a MoS_2 thermistor (Figure S6). As shown in Figure 3e,f, at relatively higher discharge rates (0.5 and 1 C), the increased heat generation raises the surface temperature of the LIB substantially, with the temperature increasing in proportion to the discharge rate up to 34.8 and 52.6°C at 0.5 and 1 C, respectively. In addition, the heat generated during charging was lower than during discharging because of the different electrochemical reactions and polarizations (voltage deviation caused by battery resistance and concentration gradient) during charging and discharging [72]. The peak temperature during charging was 31.9 and 34.8°C at 0.5 and 1 C, respectively. The battery was cycled under natural convective cooling conditions (Figure S7), which may explain the relatively high surface temperature rise observed at 0.5 C and 1 C. Throughout the charging and discharging processes, irreversible losses occur in the electrodes and electrolytes, resulting in varying internal resistances due to the differing voltages at the end of each phase. Therefore, charging and discharging generate different amounts of heat. Moreover, in the constant-current discharge and charge modes, the substantial current results in a markedly elevated heat generation rate compared with the cooling rate. Consequently, the temperature reaches its maximum at the end of the constant-current discharge and charge cycle [73, 74]. Some degree of discrepancy between the MoS_2 thermistor and the thermocouple during the pause and constant voltage charging phases could be attributed to differences in the thermal properties of the encapsulation materials used for each sensor. The MoS_2 thermistor sensitively and stably captured the temperature changes of the LIB in real time during repeated charge-discharge cycles over long periods of time. The close agreement between the temperature change results as monitored by the

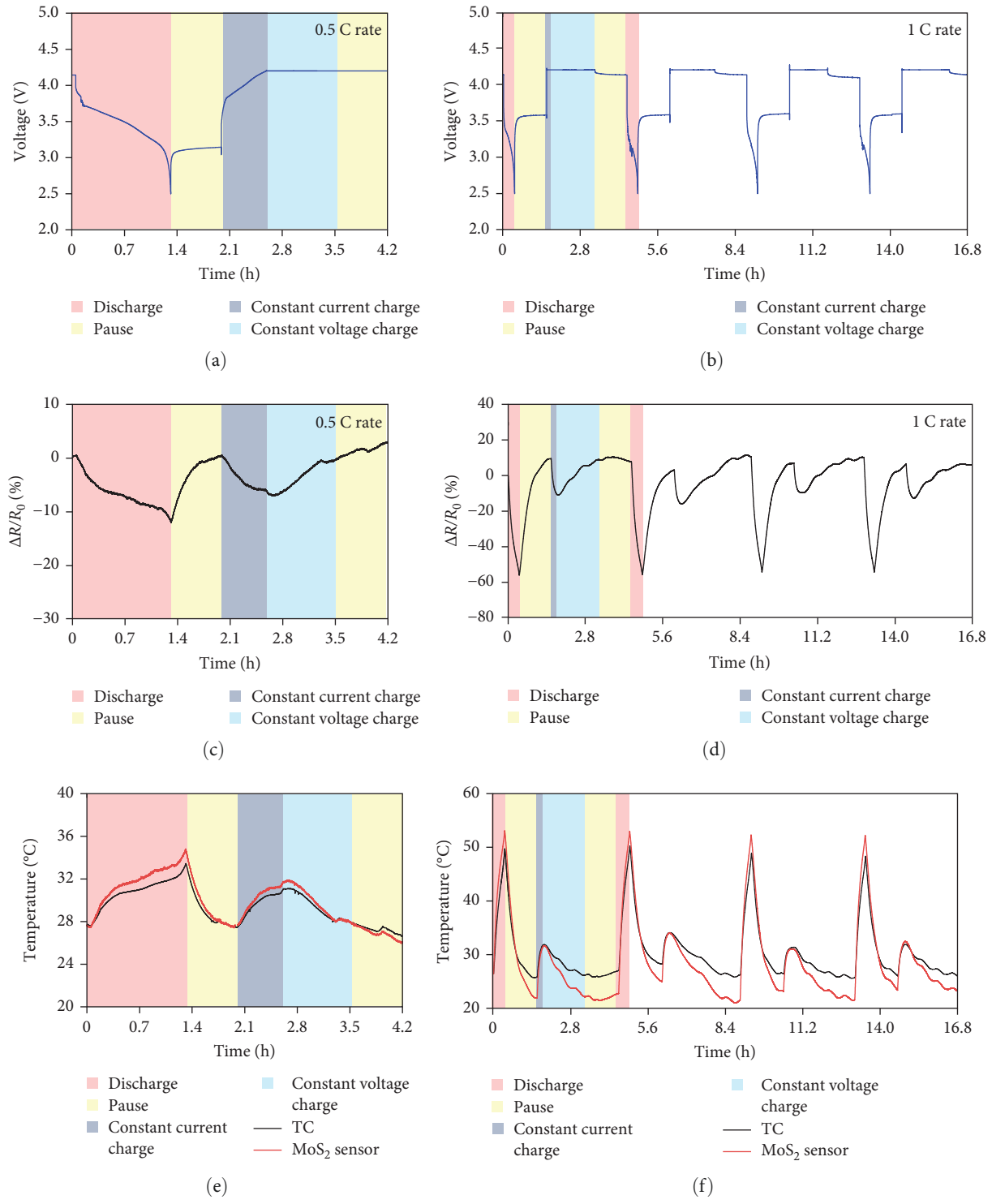

FIGURE 3: Charge and discharge cycles of LIB at (a) 0.5 C and (b) 1 C rates. Relative resistance changes of the MoS_2 thermistor during the (c) 0.5 C and (d) 1 C charge-discharge cycles. LIB temperature changes as measured by a MoS_2 thermistor and a thermocouple during the (e) 0.5 C and (f) 1 C charge-discharge cycles. The LIB temperature increases with a higher *C*-rate.

MoS_2 thermistor and the commercial thermocouple validates the capability of MoS_2 thermistors in the thermal monitoring of LIBs with improved sensitivity and adaptability. Additionally, the MoS_2 thermistor can also be applied to large-capacity LIBs, which may generate more heat during charge-discharge cycles but are typically operated within a controlled temperature range for safety and stability. The temperature changes of LIB at higher C-rates could also be measured by the MoS_2 thermistor, as it exhibited a wide detection range up to 160°C.

During charging and discharging, LIBs generate and distribute heat unevenly across the surface over time [75, 76], and local overheating may occur on the battery surface [77, 78].

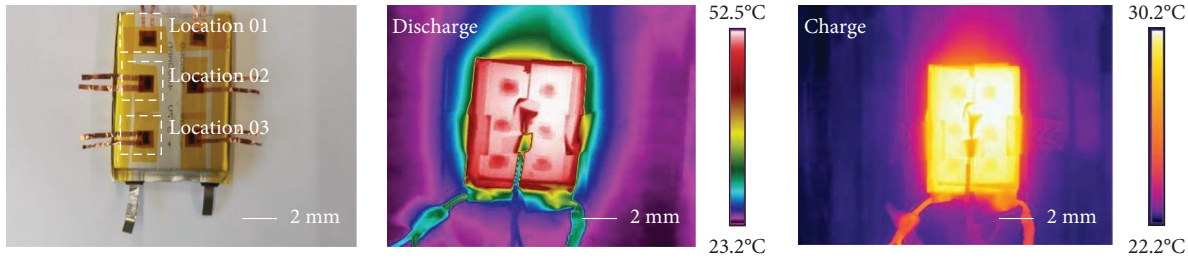

(a)

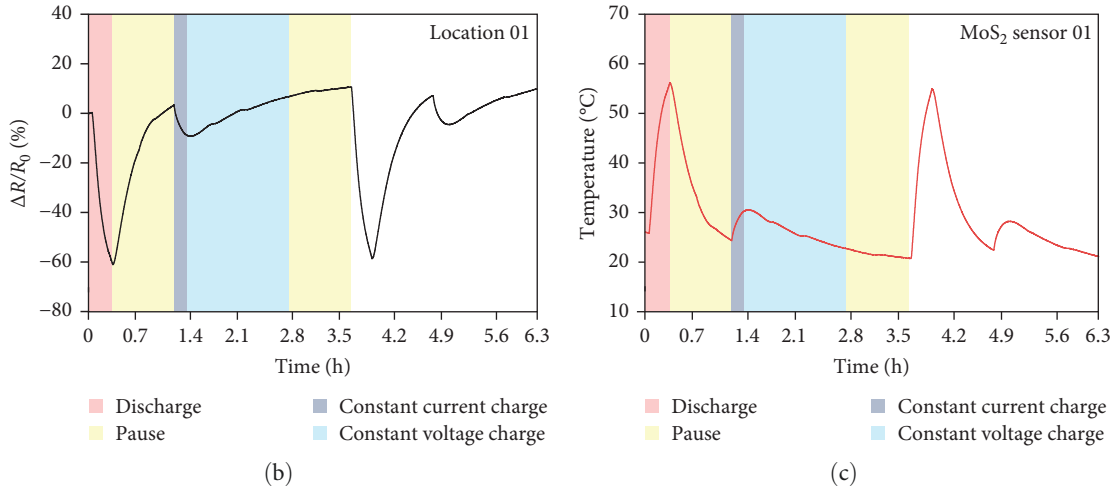

(b)

(c)

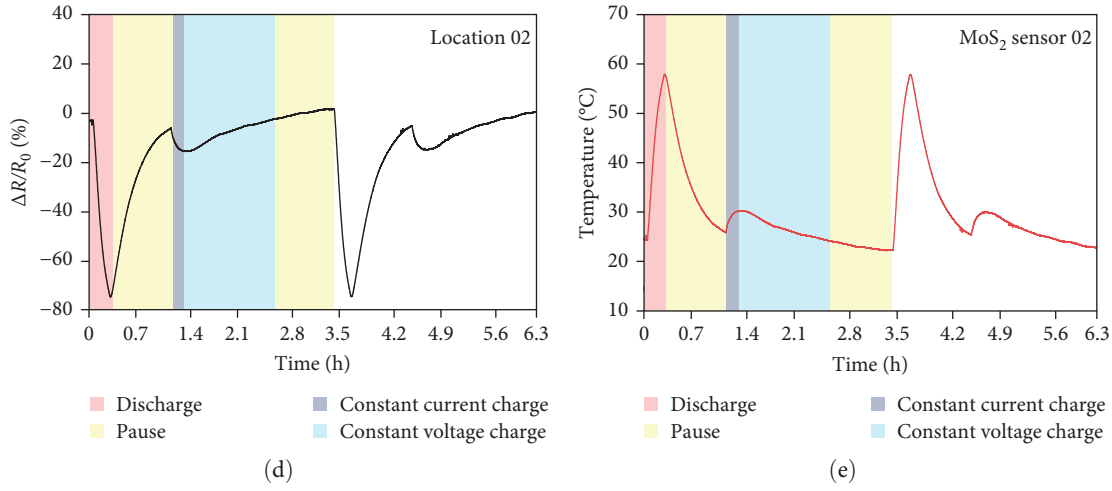

(d)

(e)

Figure 4: Continued.

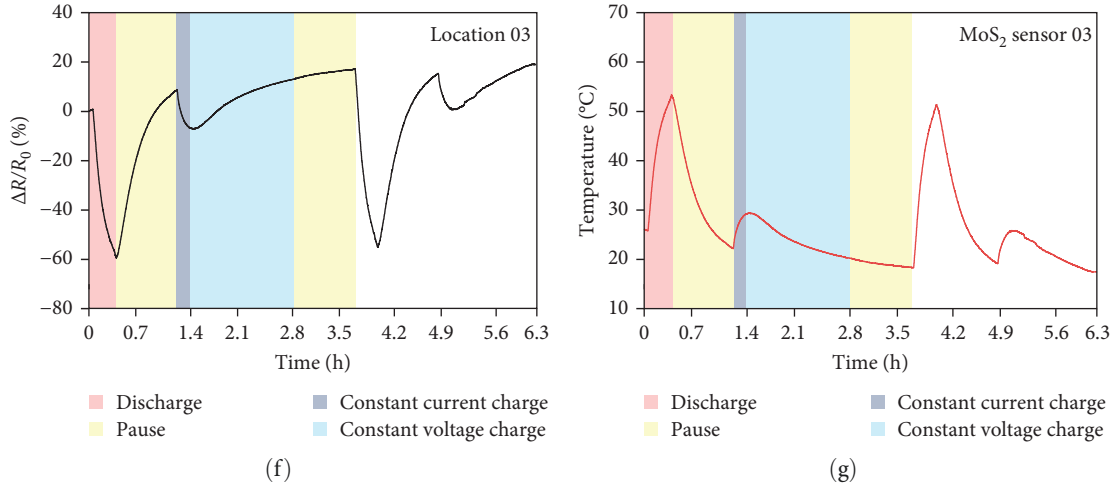

FIGURE 4: (a) Photograph of the MoS_2 thermistor-integrated LIB and corresponding IR images during discharge and charge. (b–g) Simultaneously recorded resistance changes and corresponding temperature changes of MoS_2 thermistors at different locations on the LIB surface during charge and discharge cycles.

Thus, monitoring the spatial temperature distribution is essential for the effective thermal management of LIBs. The spatial temperature distribution was measured by integrating multiple MoS_2 thermistor arrays onto the LIB surface, as shown in Figure 4a. Each thermistor simultaneously recorded the resistance change throughout the charging and discharging cycles (Figure 4b,d,f), and the resistance changes were converted to temperature (Figure 4c,e,f). The highest temperature was recorded at the end of the discharge cycle for all sensors, with the central region (Location 2) consistently exhibiting higher temperatures compared to the outer regions (Locations 1 and 3). During the outward conduction process, the outer surface of the battery is exposed to air, and heat dissipates faster, whereas the inner core retains heat, resulting in a thermal gradient [79–81]. Therefore, the highest temperature is recorded at the center of the battery surface. The lower temperature in the bottom region (Location 3) compared with the top (Location 1) was most likely a result of the improved air circulation in our setup, which enhanced heat dissipation. This central hotspot can be attributed to the accumulation of heat during prolonged discharge and the limited convection near the center region, whereas the tab-side regions experienced enhanced heat dissipation through vent openings in the test enclosure (Figure S7). Throughout the charge-discharge cycles, the measured temperature distribution aligned closely with the temperature map captured by the IR camera, confirming the accuracy of the spatial measurements by the simple MoS_2 thermistor array. As the degree of integration of the MoS_2 thermistors can be increased through microfabrication and large-area spray-coating, the spatial temperature resolution can be further improved. Our thermistor array not only successfully identified local overheating but could also be effective in preventing thermal runaway by supporting battery management systems.

4. Conclusions

A flexible MoS_2-based thermistor composed of a simple spray-coated MoS_2 nanolayer was developed and characterized. The MoS_2 thermistor exhibited excellent stability and temperature sensitivity, with a TCR of −1.94%/°C in the 20–60°C temperature range. The thermistor demonstrated a stable and measurable resistance change even with subtle temperature changes. Across multiple MoS_2 thermistors fabricated, the response deviation remained within 0.22%, with repeatability deviation below 0.04%. The MoS_2 thermistor can conformally adhere to the surface of a LIB, enabling real time temperature monitoring under various charge-discharge rates and different locations on the LIB surface, thus providing precise spatial temperature information. Experimental results and comparative analysis with conventional thermocouples and IR imaging confirmed that the MoS_2 thermistor can accurately monitor temperature fluctuations to mitigate the risk of thermal runaway in LIBs.

Data Availability Statement

The data that support the findings of this study are available from the corresponding author upon reasonable request.

Conflicts of Interest

The authors declare no conflicts of interest.

Funding

This research was supported by the Basic Science Research Program of the National Research Foundation of Korea (NRF) funded by the Ministry of Science, ICT and Future Planning (Grant RS-2023-00222166) and the Chung Ang University Young Scientist Scholarship in 2022.

Supporting Information

Additional supporting information can be found online in the Supporting Information section. (*Supporting Information*) Figure S1: The detailed fabrication process of flexible MoS_2 thermistors. Figure S2: Histogram of MoS_2 flake size measured from SEM image. Figure S3: Cross-sectional SEM image of

MoS_2 thermistor. Figure S4: TCR of various temperature-sensitive materials and TCR dependent on the mass of MoS_2 coated. Figure S5: Stability and repeatability of MoS_2 thermistor. Figure S6: Real-time temperature measurements of LIB using a MoS_2-thermistor at different C-rates. Figure S7: Schematic of experimental setup. Table S1: Comparison of the main performances of temperature sensors for LIBs. Table S2: Specifications of the LIB used in this study.

References

[1] G. E. Blomgren, "The Development and Future of Lithium Ion Batteries," *Journal of the Electrochemical Society* 164, no. 1 (2017): A5019–A5025.

[2] Y. S. Duh, K. H. Lin, and C. S. Kao, "Experimental Investigation and Visualization on Thermal Runaway of Hard Prismatic Lithium-Ion Batteries Used in Smart Phones," *Journal of Thermal Analysis and Calorimetry* 132, no. 3 (2018): 1677–1692.

[3] X. Feng, M. Ouyang, X. Liu, L. Lu, Y. Xia, and X. He, "Thermal Runaway Mechanism of Lithium Ion Battery for Electric Vehicles: A Review," *Energy Storage Materials* 10 (2018): 246–267.

[4] J.-M. Tarascon and M. Armand, "Issues and Challenges Facing Rechargeable Lithium Batteries," *Nature* 414, no. 6861 (2001): 359–367.

[5] S. Ma, M. Jiang, P. Tao, et al., "Temperature Effect and Thermal Impact in Lithium-Ion Batteries: A Review," *Progress in Natural Science: Materials International* 28, no. 6 (2018): 653–666.

[6] P. R. Tete, M. M. Gupta, and S. S. Joshi, "Developments in Battery Thermal Management Systems for Electric Vehicles: A Technical Review," *Journal of Energy Storage* 35 (2021): 102255.

[7] N. E. Galushkin, N. N. Yazvinskaya, and D. N. Galushkin, "Mechanism of Thermal Runaway in Lithium-Ion Cells," *Journal of the Electrochemical Society* 165, no. 7 (2018): A1303–A1308.

[8] Y. Ji, Y. Zhang, and C.-Y. Wang, "Li-Ion Cell Operation at Low Temperatures," *Journal of the Electrochemical Society* 160, no. 4 (2013): A636–A649.

[9] M. Xiao and S. Y. Choe, "Theoretical and Experimental Analysis of Heat Generations of a Pouch Type $LiMn_2O_4$/Carbon High Power Li-Polymer Battery," *Journal of Power Sources* 241 (2013): 46–55.

[10] L. Wang, W. Choi, K. Yoo, K. Nam, T. J. Ko, and J. Choi, "Stretchable Carbon Nanotube Dilatometer for in Situ Swelling Detection of Lithium-Ion Batteries," *ACS Applied Energy Materials* 3, no. 4 (2020): 3637–3644.

[11] S. Shahid and M. Agelin-Chaab, "A Review of Thermal Runaway Prevention and Mitigation Strategies for Lithium-Ion Batteries," *Energy Conversion and Management: X* 16 (2022): 100310.

[12] H. U. Escobar-Hernandez, R. M. Gustafson, M. I. Papadaki, S. Sachdeva, and M. S. Mannan, "Thermal Runaway in Lithium-Ion Batteries: Incidents, Kinetics of the Runaway and Assessment of Factors Affecting Its Initiation," *Journal of The Electrochemical Society* 163, no. 13 (2016): A2691–A2701.

[13] B. Mao, H. Chen, Z. Cui, T. Wu, and Q. Wang, "Failure Mechanism of the Lithium Ion Battery During Nail Penetration," *International Journal of Heat and Mass Transfer* 122 (2018): 1103–1115.

[14] J. Yang Wang, W. Bai, Z. Wang, K. Yu, Y. Lu, and C. Han, "Thermal Runaway and Jet Flame Features of LIBs Undergone High-Rate Charge/Discharge:An Investigation," *Journal of Energy Chemistry* 103 (2025): 826–837, Apr. 2025.

[15] Y. Z. Wang, Z. Wang, C. He, Y. Zhao, X. Huang, and Y. K. K. Richard, "Fire-Resistant and Mechanically-Robust Phosphorus-Doped MoS_2/Epoxy Composite as Barrier of the Thermal Runaway Propagation of Lithium-Ion Batteries," *Chemical Engineering Journal* 497 (2024): 154866.

[16] D. P. Finegan, E. Darcy, M. Keyser, et al., "Characterising Thermal Runaway Within Lithium-Ion Cells by Inducing and Monitoring Internal Short Circuits," *Energy and Environmental Science* 10, no. 6 (2017): 1377–1388.

[17] X. Zhang, S. Chen, J. Zhu, and Y. Gao, "A Critical Review of Thermal Runaway Prediction and Early-Warning Methods for Lithium-Ion Batteries," *Energy Material Advances* 4 (2023).

[18] S.-J. Lee, C.-Y. Lee, M.-Y. Chung, et al., "Lithium-Ion Battery Module Temperature Monitoring by Using Planer Home-Made Micro Thermocouples," *International Journal of Electrochemical Science* 8, no. 3 (2013): 4131–4141.

[19] D. Kong, H. Lv, P. Ping, and G. Wang, "A Review of Early Warning Methods of Thermal Runaway of Lithium Ion Batteries," *Journal of Energy Storage* 64 (2023): 107073.

[20] M. S. K. Mutyala, J. Zhao, J. Li, H. Pan, C. Yuan, and X. Li, "In-Situ Temperature Measurement in Lithium Ion Battery by Transferable Flexible Thin Film Thermocouples," *Journal of Power Sources* 260 (2014): 43–49.

[21] B. Gulsoy, T. A. Vincent, J. E. H. Sansom, and J. Marco, "In-Situ Temperature Monitoring of a Lithium-Ion Battery Using an Embedded Thermocouple for Smart Battery Applications," *Journal of Energy Storage* 54 (2022): 105260.

[22] T. J. Bajzek, "Thermocouples: A Sensor for Measuring Temperature," *IEEE Instrumentation and Measurement Magazine* 8, no. 1 (2005): 35–40.

[23] S. Wang, K. Li, Y. Tian, J. Wang, Y. Wu, and S. Ji, "Infrared Imaging Investigation of Temperature Fluctuation and Spatial Distribution for a Large Laminated Lithium-Ion Power Battery," *Applied Thermal Engineering* 152 (2019): 204–214, Apr. 2019.

[24] B. B. Kanbur, V. Kumtepeli, and F. Duan, "Thermal Performance Prediction of the Battery Surface via Dynamic Mode Decomposition," *Energy* 201 (2020): 117642–117642.

[25] J. B. Robinson, J. A. Darr, D. S. Eastwood, et al., "Non-Uniform Temperature Distribution in Li-Ion Batteries during Discharge - A Combined Thermal Imaging, X-Ray Micro-Tomography and Electrochemical Impedance Approach," *Journal of Power Sources* 252 (2014): 51–57.

[26] L. Sequino and B. M. Vaglieco, "Potential of Infrared Temperature Measurements for the Online Estimation of the State-of-Charge of a Li-Polymer Battery," *Journal of Energy Storage* 44 (2021): 103532.

[27] C. V. N. Bhaskar, S. Pal, and P. K. Pattnaik, "Recent Advancements in Fiber Bragg Gratings Based Temperature and Strain Measurement," *Results in Optics* 5 (2021): 100130.

[28] A. Fortier, M. Tsao, N. D. Williard, Y. Xing, and M. G. Pecht, "Preliminary Study on Integration of Fiber Optic Bragg Grating Sensors in Li-Ion Batteries and in Situ Strain and Temperature Monitoring of Battery Cells," *Energies* 10, no. 7 (2017): 838.

[29] S. Novais, M. Nascimento, L. Grande, et al., "Internal and External Temperature Monitoring of a Li-Ion Battery With Fiber Bragg Grating Sensors," *Sensors* 16, no. 9 (2016): 1–9.

[30] B. Li, M. H. Parekh, V. G. Pol, et al., "Operando Monitoring of Electrode Temperatures During Overcharge-Caused Thermal Runaway," *Energy Technology* 9, no. 11 (2021): 2100497.

[31] X. Ling, Q. Zhang, Y. Xiang, J. S. Chen, X. Peng, and X. Hu, "A Cu/Ni Alloy Thin-Film Sensor Integrated with Current Collector for in-Situ Monitoring of Lithium-Ion Battery Internal Temperature by High-Throughput Selecting Method," *International Journal of Heat and Mass Transfer* 214 (2023): 124383.

[32] J. A. Becker, C. B. Green, and G. L. Pearson, "Properties and Uses of Thermistors—Thermally Sensitive Resistors," *Electrical Engineering* 65, no. 11 (1946): 711–725.

[33] K. Takei, W. Honda, S. Harada, T. Arie, and S. Akita, "Toward Flexible and Wearable Human-Interactive Health-Monitoring Devices," *Advanced Healthcare Materials* 4, no. 4 (2015): 487–500.

[34] T. Yokotaa, Y. Inouea, Y. Terakawaa, et al., "Ultraflexible, Large-Area, Physiological Temperature Sensors for Multipoint Measurements," *Proceedings of the National Academy of Sciences* 112, no. 47 (2015): 14533–14538.

[35] A. Di Bartolomeo, M. Sarno, F. Giubileo, et al., "Multiwalled Carbon Nanotube Films as Small-Sized Temperature Sensors," *Journal of Applied Physics* 105, no. 6 (2009).

[36] A. Giuliani, M. Placidi, F. Di Francesco, and A. Pucci, "A New Polystyrene-Based Ionomer/MWCNT Nanocomposite for Wearable Skin Temperature Sensors," *Reactive and Functional Polymers* 76 (2014): 57–62.

[37] G. Liu, Q. Tan, H. Kou, et al., "A Flexible Temperature Sensor Based on Reduced Graphene Oxide for Robot Skin Used in Internet of Things," *Sensors* 18, no. 5 (2018): 1400.

[38] Z. Cui, F. R. Poblete, and Y. Zhu, "Tailoring the Temperature Coefficient of Resistance of Silver Nanowire Nanocomposites and Their Application as Stretchable Temperature Sensors," *ACS Applied Materials and Interfaces* 11, no. 19 (2019): 17836–17842.

[39] R. Srivastava, "Investigation on Temperature Sensing of Nanostructured Zinc Oxide Synthesized via Oxalate Route," *Journal of Sensor Technology* 02, no. 1 (2012): 8–12.

[40] B. Sun, G. Xu, X. Ji, et al., "A Strain-Resistant Flexible Thermistor Sensor Array Based on CNT/MXene Hybrid Materials for Lithium-Ion Battery and Human Temperature Monitoring," *Sensors and Actuators A: Physical* 368 (2024): 115059.

[41] A. I. Khan, P. Khakbaz, K. A. Brenner, et al., "Large Temperature Coefficient of Resistance in Atomically Thin Two-Dimensional Semiconductors," *Applied Physics Letters* 116, no. 20 (2020).

[42] J. S. Kim, J. Kim, J. Zhao, et al., "Electrical Transport Properties of Polymorphic MoS_2," *ACS Nano* 10, no. 8 (2016): 7500–7506.

[43] J. Choi, H. Zhang, and J. H. Choi, "Modulating Optoelectronic Properties of Two-Dimensional Transition Metal Dichalcogenide Semiconductors by Photoinduced Charge Transfer," *ACS Nano* 10, no. 1 (2016): 1671–1680.

[44] J. Mohanraj, V. Velmurugan, S. Sathiyan, and S. Sivabalan, "All Fiber-Optic Ultra-Sensitive Temperature Sensor Using Few-Layer MoS_2 Coated D-Shaped Fiber," *Optics Communications* 406 (2018): 139–144.

[45] F. Khan, C. M. Julien, and S. S. Islam, "Fabrication of Multiwalled Carbon Nanotubes/MoS_2 Nanocomposite: Application as Temperature Sensor," *FlatChem* 40 (2023): 100521.

[46] Y. Xie, T. M. Chou, W. Yang, et al., "Flexible Thermoelectric Nanogenerator Based on the MoS_2/Graphene Nanocomposite and Its Application for a Self-Powered Temperature Sensor," *Semiconductor Science and Technology* 32, no. 4 (2017): 044003.

[47] A. Daus, M. Jaikissoon, A. I. Khan, et al., "Fast-Response Flexible Temperature Sensors With Atomically Thin Molybdenum Disulfide," *Nano Letters* 22, no. 15 (2022): 6135–6140.

[48] A. Jawaid, D. Nepal, K. Park, et al., "Mechanism for Liquid Phase Exfoliation of MoS_2," *Chemistry of Materials* 28, no. 1 (2016): 337–348.

[49] X. Cong, X. L. Liu, M. L. Lin, and P. H. Tan, "Application of Raman Spectroscopy to Probe Fundamental Properties of Two-Dimensional Materials, Npj 2D," *Materials and Applications* 4, no. 1 (2020).

[50] R. T. Sam, T. Umakoshi, and P. Verma, "Probing Stacking Configurations in a Few Layered MoS_2 by Low Frequency Raman Spectroscopy," *Scientific Reports* 10, no. 1 (2020).

[51] X. Ling, L. Liang, S. Huang, et al., "Low-Frequency Interlayer Breathing Modes in Few-Layer Black Phosphorus," *Nano Letters* 15, no. 6 (2015): 4080–4088.

[52] X. Zhang, X. F. Qiao, W. Shi, J. Bin Wu, D. S. Jiang, and P. H. Tan, "Phonon and Raman Scattering of Two-Dimensional Transition Metal Dichalcogenides From Monolayer, Multilayer to Bulk Material," *Chemical Society Reviews* 44, no. 9 (2015): 2757–2785.

[53] R. Shahzad, T. W. Kim, and S. W. Kang, "Effects of Temperature and Pressure on Sulfurization of Molybdenum Nano-Sheets for MoS_2 Synthesis," *Thin Solid Films* 641 (2017): 79–86.

[54] M. D. Siao, W. C. Shen, R. S. Chen, et al., "Two-Dimensional Electronic Transport and Surface Electron Accumulation in MoS_2," *Nature Communications* 9, no. 1 (2018): 1442.

[55] G. Zhang and Y. W. Zhang, "Thermoelectric Properties of Two-Dimensional Transition Metal Dichalcogenides," *Journal of Materials Chemistry C* 5, no. 31 (2017): 7684–7698.

[56] H. Qiu, T. Xu, Z. Wang, et al., "Hopping Transport through Defect-Induced Localized States in Molybdenum Disulphide," *Nature Communications* 4, no. 1 (2013): 2642.

[57] V. Gunasekaran, M. K. Devaraju, S. Yuvaraj, et al., "Electrical Transport Properties of Two-Dimensional MoS_2 Nanosheets Synthesized by Novel Method," *Materials Science in Semiconductor Processing* 66 (2017): 81–86.

[58] T. S. Ko, E. T. Lin, X. W. Huang, P. T. Wu, and Y. L. Yang, "High-Temperature Coefficient of Resistance in $MoxW_{1-x}S_2$ Thin Film," *Applied Sciences* 12, no. 10 (2022): 5110.

[59] S. Mukherjee, S. Biswas, A. Ghorai, A. Midya, S. Das, and S. K. Ray, "Tunable Optical and Electrical Transport Properties of Size- and Temperature-Controlled Polymorph MoS_2 Nanocrystals," *Journal of Physical Chemistry C* 122, no. 23 (2018): 12502–12511.

[60] H. J. Kwon, J. Jang, S. Kim, V. Subramanian, and C. P. Grigoropoulos, "Electrical Characteristics of Multilayer MoS_2 Transistors at Real Operating Temperatures With Different Ambient Conditions," *Applied Physics Letters* 105, no. 15 (2014).

[61] G. Bree, H. Hao, Z. Stoeva, and C. T. John Low, "Monitoring State of Charge and Volume Expansion in Lithium-Ion Batteries: An Approach Using Surface Mounted Thin-Film Graphene Sensors," *RSC Advances* 13, no. 10 (2023): 7045–7054.

[62] T. Zheng, M. Muneeswara, H. Bao, et al., "Gas Evolution in Li-Ion Rechargeable Batteries: A Review on Operando Sensing Technologies, Gassing Mechanisms, and Emerging Trends," *ChemElectroChem* 11, no. 15 (2024): e202400065.

[63] D. S. Schulman, D. May-Rawding, F. Zhang, D. Buzzell, N. Alem, and S. Das, "Superior Electro-Oxidation and Corrosion Resistance of Monolayer Transition Metal Disulfides," *ACS Applied Materials and Interfaces* 10, no. 4 (2018): 4285–4294.

[64] S. Ren, Y. Shi, C. Zhang, M. Cui, and J. Pu, "Anomalous Enhancement Oxidation of Few-Layer MoS2 and MoS2/h-BN Heterostructure," *Nano Research* 15, no. 8 (2022): 7081–7090.
[65] J. Newman, K. E. Thomas, H. Hafezi, and D. R. Wheeler, "Modeling of Lithium-Ion Batteries," *Journal of Power Sources* 119–121 (2003): 838–843.
[66] R. E. Williford, V. V. Viswanathan, and J. G. Zhang, "Effects of Entropy Changes in Anodes and Cathodes on the Thermal Behavior of Lithium Ion Batteries," *Journal of Power Sources* 189, no. 1 (2009): 101–107.
[67] Z. Yunyun, Z. Guoqing, W. Weixiong, and L. Weixiong, "Heat Dissipation Structure Research for Rectangle LiFePO4 Power Battery," *Heat and Mass Transfer* 50, no. 7 (2014): 887–893.
[68] X. Bai, H. Jin, C. Duan, Y. Gao, A. Nakayama, and C. Liu, "Simulation Study on Heat Dissipation of a Prismatic Power Battery Considers Anisotropic Thermal Conductivity in Air Cooling System," *Thermal Science and Engineering Progress* 55 (2024): 102920.
[69] M. Usman Tahir, A. Sangwongwanich, D.-I. Stroe, and F. Blaabjerg, "Overview of Multi-Stage Charging Strategies for Li-Ion Batteries," *Journal of Energy Chemistry* 84 (2023): 228–241.
[70] R. Christen, G. Rizzo, A. Gadola, and M. Stöck, "Test Method for Thermal Characterization of Li-Ion Cells and Verification of Cooling Concepts," *Batteries* 3, no. 1 (2017): 3.
[71] W. Mei, H. Li, C. Zhao, J. Sun, and Q. Wang, "Numerical Study on Thermal Characteristics Comparison Between Charge and Discharge Process for Lithium Ion Battery," *International Journal of Heat and Mass Transfer* 162 (2020): 120319.
[72] K. Kumaresan, G. Sikha, and R. E. White, "Thermal Model for a Li-Ion Cell," *Journal of The Electrochemical Society* 155, no. 2 (2008): A164.
[73] X.-D. Yuan, D.-M. Qian, X.-Y. Wang, et al., "Numerical Research on Electrochemical Behavior, Thermal Characteristics, and Aging Formation of Lithium-Ion Cell at Different Ambient Temperatures and Charge/Discharge Rates," *Energy and Fuels* 38, no. 21 (2024): 21554–21574.
[74] G. Liu, M. Ouyang, L. Lu, J. Li, and X. Han, "Analysis of the Heat Generation of Lithium-Ion Battery during Charging and Discharging considering Different Influencing Factors," *Journal of Thermal Analysis and Calorimetry, Kluwer Academic Publishers* 116, no. 2 (2014): 1001–1010.
[75] Y. Ye, Y. Shi, N. Cai, J. Lee, and X. He, "Electro-Thermal Modeling and Experimental Validation for Lithium Ion Battery," *Journal of Power Sources* 199 (2012): 227–238.
[76] Y. Zheng, Y. Che, X. Hu, X. Sui, D. I. Stroe, and R. Teodorescu, "Thermal State Monitoring of Lithium-Ion Batteries: Progress, Challenges, and Opportunities," *Progress in Energy and Combustion Science* 100 (2024): 101120.
[77] S. Goutam, A. Nikolian, J. Jaguemont, et al., "Three-Dimensional Electro-Thermal Model of Li-Ion Pouch Cell: Analysis and Comparison of Cell Design Factors and Model Assumptions," *Applied Thermal Engineering* 126 (2017): 796–808.
[78] X. Zhang, X. Chang, Y. Shen, and Y. Xiang, "Electrochemical-Electrical-Thermal Modeling of a Pouch-Type Lithium Ion Battery: An Application to Optimize Temperature Distribution," *Journal of Energy Storage* 11 (2017): 249–257.
[79] H. Lundgren, P. Svens, H. Ekström, et al., "Thermal Management of Large-Format Prismatic Lithium-Ion Battery in PHEV Application," *Journal of the Electrochemical Society* 163, no. 2 (2015): A309–A317.
[80] J. Yang, H. Zhang, Y. Xu, and P. Li, "Analysis of Heat Generation in Lithium-Ion Battery Components and Voltage Rebound Based on Electrochemical and Thermal Coupled Model," *Journal of Energy Storage* 72 (2023): 108554.
[81] J. Zhang, X. G. Yang, F. Sun, Z. Wang, and C. Y. Wang, "An Online Heat Generation Estimation Method for Lithium-Ion Batteries Using Dual-Temperature Measurements," *Applied Energy* 272 (2020): 115262.